Chinese Physics Letters

LETTER

State-to-State Dynamics Study on the C(^{1}D)+HD (v = 1, j = 2) Insertion Reaction: Isotope Effects and Stereodynamical Control

Cite as: Wenqian Li *et al*. 2026 *Chin. Phys. Lett.* **43** 090303

DOI CSTR

Recommended Articles

Theoretical Study of Isotopic Effect of Oxygen Atom on the Stereodynamics for the O(^{3}P)+ D_2 → OD+D Reaction
LIU Shi-Li, and SHI Ying
Chin. Phys. Lett. **27**, 123103 (2010)

Influence of Isotope Effects on the Stereodynamics of the N(^4S)+H_2 → NH+H Reactive System: a QCT Study
ZHANG Juan, CHU Tian-Shu, DONG Shun-Le, YUAN Shu-Ping, FU Ai-Ping, and DUAN Yun-Bo
Chin. Phys. Lett. **28**, 093403 (2011)

Theoretical Exploration of the Isotopic Effect on Nuclear Dynamics in Coulomb Explosion
SHI Hao-Ting, and MIAO Xiang-Yang
Chin. Phys. Lett. **30**, 063101 (2013)

Quasiclassical-Trajectory Investigation on the Isotopic Effect of H(D)+LiF→H(D)F+Li (v=0–4, j=0) Reaction
XIE Ting-Xian, ZHANG Ying-Ying, SHI Ying, and JIN Ming-Xing
Chin. Phys. Lett. **32**, 098201 (2015)

Effect of Rotational Excitation on Stereodynamics for the Reactive Collision Between N(^{2}D) and H_2
CHENG Jie, YUE Xian-Fang, and FENG Hai-Ran
Chin. Phys. Lett. **29**, 043101 (2012)

A series journal of Chinese Physical Society distributed by IOP Publishing

Chinese Physics Letters

Chin. Phys. Lett. **43** 090303 (2026)

LETTER

DOI: 10.1088/0256-307X/43/9/090303
CSTR: 32039.14.0256-307X.43.9.090303

State-to-State Dynamics Study on the C(^{1}D)+HD ($v = 1, j = 2$) Insertion Reaction: Isotope Effects and Stereodynamical Control

Wenqian Li(李文茜)[1], Xiaoxi Xu(许晓曦)[2,*], Zeya Wang(王泽亚)[1], Jie Yu(于杰)[1,*], and Maodu Chen(陈茂笃)[1,*]

[1]Key Laboratory of Materials Modification by Laser, Electron, and Ion Beams (Ministry of Education), School of Physics, Dalian University of Technology, Dalian 116024, China
[2]College of Physics, Chengdu University of Technology, Chengdu 610059, China

*Corresponding authors. Email: xiaoxi_xu@cdut.edu.cn; yujie@dlut.edu.cn; mdchen@dlut.edu.cn

The isotope effects and stereodynamical control in the C(^{1}D)+HD (v = 1, j = 2) insertion reaction are investigated using the time-dependent wave packet method, based on a high-precision neural network potential energy surface of $CH_2(\tilde{a}^1A')$. The reaction probabilities at J = 0 exhibit no threshold and show pronounced resonance oscillations. Integral cross sections reveal that the CD+H channel dominates at low collision energies due to contributions from low partial waves. However, the CH+D channel becomes dominant above 0.43 eV as high partial waves take over, leading to an inversion of the product branching ratio. Stereodynamical analysis reveals that the parallel configuration significantly enhances the CH+D channel, while the perpendicular configuration suppresses it and weakly promotes the CD+H channel. Furthermore, the parallel alignment enhances forward and backward scattering for both product channels. Specifically, aligning the HD molecule parallel to the relative velocity lowers the critical collision energy required for CH+D dominance, thereby significantly amplifying its competitive advantage over the CD+H channel.

Isotope effects play a pivotal role in chemical physics, providing deeper insights into reaction dynamics [1–4]. Among isotope-substitution reactions, the C+HD reaction, as a prototypical insertion system [5–8], has attracted sustained experimental and theoretical attention. The interactions between carbon atoms and hydrogen molecules together with their isotopic variants have been extensively investigated both experimentally and theoretically.

Experimentally, Fisher *et al.* [9] first measured the CD/CH branching ratio using laser-induced fluorescence, reporting a value of 1.69 ± 0.07 at collision energies below 4.2 kJ/mol and highlighting the preferential formation of CD+H products. Sato *et al.* [10] later determined room-temperature rate constants for reactions of C(^{1}D) with H_2, HD, and D_2 using a pump-probe method, yielding a total rate constant of $(1.7 \pm 0.4) \times 10^{-10}$ cm$^3\cdot$s^{-1} for C+HD and a branching ratio of 1.6 ± 0.1, confirming the dominance of the CD+H channel. More recently, Wu *et al.* [8] employed a continuous supersonic flow reactor to measure rate constants and branching ratios over 50–296 K, revealing a pronounced negative temperature dependence of the branching ratio at low temperatures and providing critical constraints for mechanistic understanding. Theoretically, continuous advancements in potential energy surfaces (PES) and dynamical methods have enabled quantitative descriptions of the C+HD reaction. Bussery-Honvault *et al.* [11] developed the global ab initio BHL PES for $CH_2(\tilde{a}^1A')$, demonstrating that the vertical insertion pathway is barrierless while the collinear abstraction pathway exhibits a barrier of ~0.54 eV, confirming insertion as the dominant mechanism. Using this PES, Lin and Guo [12] performed Chebyshev wave packet calculations and observed dense resonance structures supported by the deep CH_2 well, with predicted rate constants and branching ratios in good agreement with experiments. Defazio *et al.* [13] further reported state-to-state integral and differential cross sections for the C(^{1}D)+HD reaction on the $\tilde{a}^1A'$ and $\tilde{b}^1A''$ electronic states, and observed abundant sharp resonance structures on the two PESs. Joseph *et al.* [14] reported reactivity trends $k(H_2) > k(HD) > k(D_2)$ from quasi-classical trajectory calculations. Bian's group constructed high-precision ZMB-a [15,16] and ZMB-b PESs and identified an intermediate whose dynamics are modulated by a conical intersection [8,17], which induces selective C-H activation and amplifies the CD/CH branching ratio via two non-statistical dynamical pathways. Very recently, Liu *et al.* [18] constructed a global neural-network PES for $CH_2(\tilde{a}^1A')$, providing an improved theoretical benchmark for studying isotope effects in C+HD.

In recent years, stereodynamics has emerged as a frontier in molecular reaction dynamics, aiming to unravel the vector correlations in chemical collisions [19] and offering the potential to control reaction outcomes via precise manipulation of reactant alignment [20–22]. The Stark-induced adiabatic Raman passage (SARP) technique [23], capable of preparing reactants in specific quantum states such as HD in the $v = 1, j = 2$ level, has been successfully applied to numerous non-reactive inelastic scattering processes [24,25]. Complementing these SARP-based non-reactive studies, Wang *et al.* [26] recently achieved stereodynamical control of a reactive bimolecular process, reporting a high-resolution investigation of H+HD using polarized stimulated Raman pumping (SRP). Their work provided compelling evidence that manipulating the initial reactant configuration can effectively steer chemical outcomes. Despite these experimental strides, theoretical explorations of stereodynamics in the C(^{1}D)+H_2/HD system remain relatively scarce. While early quasi-classical trajectory (QCT) studies by Kang [27] provided some initial insights into product polarization at specific collision energies, a comprehensive theoretical understanding of the stereodynamical mechanisms in this insertion reaction is still lacking. Given the complex non-statistical dynamics and the deep potential well involved [8,18], further theoretical investigation is essential to interpret the vector correlations and isotope effects. Experimentally, mature techniques are available for preparing HD ($v = 1, j = 2$) with a purity sufficient for small-molecule reaction studies, and this excited molecular system has been widely applied in stereodynamical experiments [26,28], providing an experimentally accessible benchmark for theoretical investigation. In this work, we present a comprehensive time-dependent wave packet investigation of isotope effects and stereodynamical control in the C+HD ($v = 1, j = 2$) insertion reaction, performed on a high-precision neural network potential energy surface, to elucidate the underlying

Received 16 July 2026; accepted 17 August 2026; published 7 September 2026
© 2026 Chinese Physical Society and IOP Publishing Ltd. All rights, including for text and data mining, AI training, and similar technologies, are reserved.

Check for updates

Table 1. Main parameters used in the quantum TDWP method.

C(^{1}D)+HD ($v = 1, j = 2$) → CD/CH + H/D	
Grid/basis range and size[a]	R (bohr) ∈ [0.1, 16.0], $N_R^{tot} = 225$, $N_R^{int} = 125$ r (bohr) ∈ [0.1, 16.0], $N_r^{tot} = 149$, $N_r^{asy} = 79$ $j_{max} = 150$
Initial wave pack $\exp\left[-\frac{(R-R_c)^2}{r^2} - ik_0R\right]$	$R_c = 11.0$ bohr, $\tau = 0.22$ bohr $k_0 = \sqrt{2\mu_R E_0}$ with $E_0 = 0.50$ eV
Total propagation time	50000 a.u.
Time step	5.0 a.u.
Collision energy	$E_{min} = 0.01$ eV, $E_{max} = 0.60$ eV, $N_E = 200$
Highest J value	64
Absorbing potential	$R: C_a = 0.10, R_a = 12.5, C_b = 0.50, R_b = 15.5, n_R = 2.0$ $r: C_a = 0.12, R_a = 12.4, C_b = 0.50, R_b = 14.0, n_r = 2.0$

[a] N_R^{tot} and N_r^{tot} are the number of grid points and N_E is the number of collision energy grid points. j_{max} is the maximum rotational basis, which is used for the interaction region.

mechanisms governing vector correlations and product branching ratios.

The state-to-state quantum dynamics calculations for the C(^{1}D)+HD reaction were carried out using the time-dependent wave packet (TDWP) method [29,30]. This study is based on a high-precision neural network potential energy surface for the $CH_2(\tilde{a}^1A')$ ground state [18], which provides a reliable platform for investigating the intricate dynamics of this insertion reaction.

The calculations were performed in the reactant Jacobi coordinates (r, R, θ), where r denotes the internuclear distance of the HD molecule, R represents the distance from the C atom to the center of mass of HD, and θ is the angle between the vectors R and r. Within this coordinate framework, the total Hamiltonian of the system is expressed as

$$\hat{H} = -\frac{\hbar^2}{2\mu_R}\frac{\partial^2}{\partial R^2} - \frac{\hbar^2}{2\mu_r}\frac{\partial^2}{\partial r^2} + \frac{\hat{j}^2}{2\mu_r r^2} + \frac{\left(\hat{J}-\hat{j}\right)^2}{2\mu_R R^2} + \hat{V}(r,R,\theta), \quad (1)$$

where μ_R and μ_r represent the corresponding reduced masses for R and r, $\hat{J}$ is the total angular momentum operator of the C-HD system, and $\hat{j}$ is the rotational angular momentum operator of the HD molecule. The interaction potential V (r, R, θ) excludes the reference energy of the isolated HD molecule.

The propagation of the initial wave packet was carried out using the second-order split-operator scheme combined with the Fourier grid method [29–31]. To ensure numerical stability and accuracy, the discrete variable representation (DVR) method was utilized for the potential energy operator, while the fast Fourier transform (FFT) technique was employed to handle the radial kinetic energy operators [32,33]. A complex absorbing potential (CAP) was applied at the grid boundaries to eliminate unphysical reflections arising from the finite grid range [33–35].

After propagation, the state-to-state reactive ***S***-matrix elements were extracted in the space-fixed (SF) frame using the reactant-coordinate-based (RCB) method proposed by Sun *et al.* [36–38], which allows for the direct calculation of scattering attributes from wave packets in reactant Jacobi coordinates without the need for coordinate transformation. These ***S***-matrix elements serve as the foundation for calculating various scattering observables, including differential and integral cross sections.

A key focus of this work is the stereodynamical control of the reaction outcome. The state-to-state scattering amplitude under specific stereodynamical configurations can be derived from the ***S***-matrix. Following the formalism based on the Wigner rotation matrices [39] and the theoretical framework for vector correlations [13,26], the spatial configuration of the HD molecule is described by the superposition of states with different magnetic quantum numbers (m).

For the parallel configuration ($\beta = 0°$), where the HD bond axis is aligned parallel to the relative velocity vector, the differential cross section (DCS) is given by

$$\begin{aligned}\frac{d\sigma_{v'j'm'\leftarrow v=1,j=2,m_z=0}(\theta,E)}{d\Omega} &= \left|f^{Para}(\theta,E)\right|^2 \\ &= \left|f_{v'j'm'\leftarrow v=1,j=2,m_z=0}(\theta,E)\right|^2 \\ &= \left|f_{m'\leftarrow m=0}(\theta,E)\right|^2.\end{aligned} \quad (2)$$

For the perpendicular configuration ($\beta = 90°$), where the HD bond axis is aligned perpendicular to the relative velocity vector, the DCS involves the coherent superposition of $m = \pm 2$ channels:

$$\begin{aligned}&\frac{d\sigma_{v'j'm'\leftarrow v=1,j=2,m_x=0}(\theta,E)}{d\Omega} \\ &= \left|f^{Perp}(\theta,E)\right|^2 \\ &= \left|\sqrt{\frac{3}{8}}f_{m'\leftarrow m=2}(\theta,E) - \frac{1}{2}f_{m'\leftarrow m=0}(\theta,E) + \sqrt{\frac{3}{8}}f_{m'\leftarrow m=-2}(\theta,E)\right|^2.\end{aligned} \quad (3)$$

The state-to-state integral cross section (ICS) is then derived by integrating the DCS over all solid angles:

$$\sigma_{v'j'\leftarrow vj}(E) = \int \frac{d\sigma}{d\Omega}(\theta)\,d\Omega. \quad (4)$$

This theoretical framework allows us to precisely manipulate the spatial alignment of the reactant HD molecule and investigate the resulting vector correlations in the product distribution.

Owing to the distinctive isotope effects of the HD molecule, its reaction dynamics has attracted considerable attention. The present work employs the global $CH_2(\tilde{a}^1A')$ PES recently constructed by Liu *et al.* [18], here applied to the C(^{1}D)+HD isotopologue. The construction and salient features of this surface are detailed in Ref. [18]. For the dynamics, we adopt the TDWP method. To balance computational cost against convergence, the numerical parameters were optimized from convergence tests on the $J = 0$ reaction probabilities and subsequently verified at $J = 10$ and $J = 20$. The final parameters, adopted for all $J > 0$ calculations, are summarized in Table 1.

Before presenting the dynamical results, we outline the essential topological features of the PES governing the title reaction. Figure 1 depicts the minimum-energy path along the reaction coordinate for C(^{1}D)+HD on the $CH_2(\tilde{a}^1A')$ PES. The dominant pathway is a strictly barrierless perpendicular (C-H-D) insertion: the incoming C(^{1}D) atom inserts into the H-D bond near a T-shaped geometry and descends monotonically into a deep $CH_2(\tilde{a}^1A')$ well (~4.4 eV below the reactant asymptote). From this well the system dissociates to either the CH+D or the CD+H product channel, both of which are highly

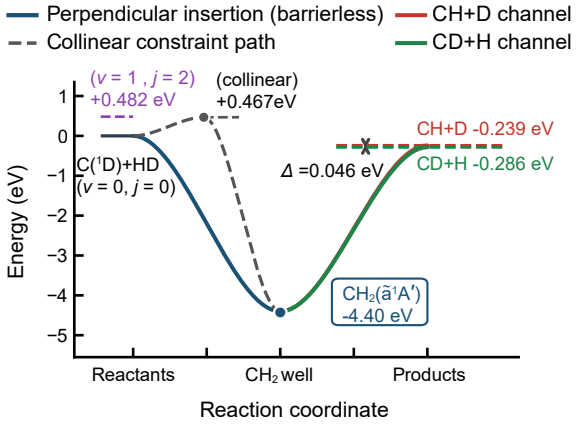

Fig. 1. Reaction pathway diagram for the C(^{1}D)+HD ($v = 1, j = 2$) → CD/CH+D/H reaction on the $CH_2(\tilde{a}^1A')$ PES. The perpendicular insertion pathway is shown as a solid blue curve, the collinear abstraction pathway (with a barrier) as a dashed gray curve, and the two product channels are indicated.

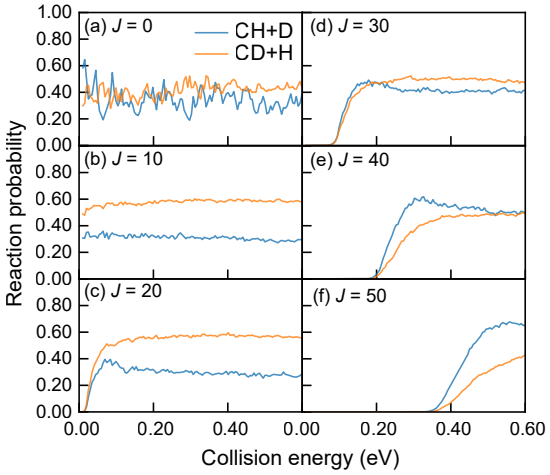

Fig. 2. Total reaction probabilities of the two channels of the C(^{1}D)+HD ($v = 1, j = 2$) → CD/CH+D/H reaction in the collision energy range from 0.01 to 0.60 eV at selected partial waves ($J = 0$, 10, 20, 30, 40, 50).

exothermic. The CD+H channel lies lower by $\Delta = 0.046$ eV, reflecting the lower zero-point energy of the C-D versus C-H bond. In contrast, a collinear (H-D-C) approach encounters an ~0.47 eV barrier [18] that suppresses reactivity at low collision energies. The HD ($v = 1, j = 2$) initial state lies ~0.48 eV above the HD ground state. This energy is just above the collinear barrier.

Figure 2 shows the total reaction probabilities for the C(^{1}D)+HD ($v = 1, j = 2$) → CD/CH+H/D reaction within the collision energy range of 0.01–0.60 eV for six partial waves. Both product channels exhibit similar overall behaviors. For both CH and CD products, no reaction threshold is observed at $J = 0$ consistent with the barrierless, exothermic character of the reaction. Pronounced oscillations appear due to the deep potential well that supports a long-lived H-C-D complex and numerous resonance states. As J increases, the reaction threshold rises, the curves smooth out, and resonance features weaken, because the centrifugal barrier reduces the effective well depth. The two channels exhibit distinct differences with increasing J. At $J = 0$, CD+H is more favorable at very low energies. At $J = 10$, CD+H remains dominant. At $J = 20$, both channels show a threshold near $E_c = 0.02$ eV. At $J = 30$, their probability difference decreases. At $J = 40$, the CH+D channel becomes dominant. To ensure converged integral cross sections, calculations were extended to a maximum total angular momentum of $J_{max} = 64$. The reaction probabilities for $J_{max} = 64$ remain negligible across the entire collision energy range due to complete suppression by the centrifugal barrier, confirming that the partial wave expansion is well converged.

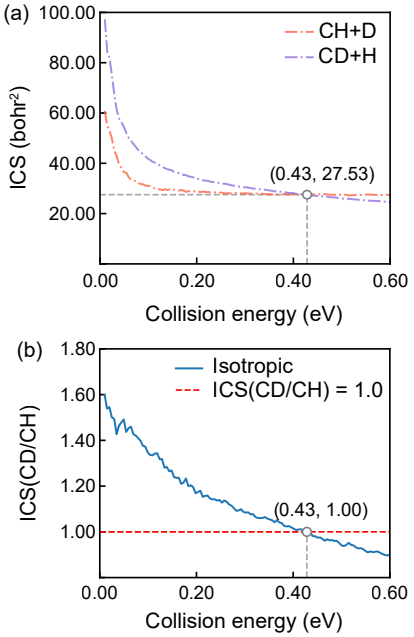

Fig. 3. (a) Total ICSs of the C(^{1}D)+HD ($v = 1, j = 2$) → CD/CH+D/H reaction and (b) the CD/CH branching ratio as a function of collision energy.

Figure 3(a) presents the total ICSs for the C(^{1}D)+HD ($v = 1, j = 2$) → CH+D and CD+H reaction. The total ICSs for both channels decrease rapidly with increasing collision energy, consistent with the barrierless insertion mechanism. Unlike previous studies that reported persistent dominance of the CD+H channel [12,40,41], we find that the CH+D ICS plateaus at high energies while the CD+H ICS decreases slightly, narrowing the gap between the two channels. Above $E_c = 0.43$ eV, the CH+D channel becomes dominant. As indicated in Fig. 2, low partial waves ($J = 10$) favor CD+H at low energies, whereas high partial waves ($J = 40$, 50) favor CH+D at high energies, leading to the observed dominance reversal. Figure 3(b) shows the CD/CH branching ratio for the intramolecular isotope effect. It exhibits oscillatory features and decreases overall with increasing collision energy. We attribute this difference to the excitation of the reactant HD. Previous calculations on the ground electronic state employed ground-state HD ($v = 0, j = 0$) and consistently reported a persistent CD+H dominance (CD/CH>1) [12,40–42], whereas the present work uses HD in the ($v = 1, j = 2$) state and observes a reversed preference for the CH+D channel above $E_c = 0.43$ eV (CD/CH<1). It has been demonstrated in several reactions that an excited reactant markedly alters the product branching ratio [4,43].

Figure 4 shows the rotationally resolved integral cross sections for the C(^{1}D)+HD ($v = 1, j = 2$) reaction at collision energies $E_c = 0.05$, 0.20, 0.40, and 0.60 eV. Panels (a)–(d) are for the CH+D channel, and panels (e)–(h) for the CD+H channel. For both channels, lower vibrational states access higher rotational levels compared to higher vibrational states. As collision energy increases, both channels populate higher vibrational and rotational states due to enhanced internal energy deposition, with this effect being more pronounced in the CD+H channel. At $E_c = 0.20$ eV, both channels show clear peaks for $v' = 0$ and 1. The CD+H channel has slightly lower peaks but broader rotational distributions, yielding larger total ICS for $v' = 0$, 1, and 2 compared to CH+D. At $E_c = 0.60$ eV, the peak intensities of CD+H for $v' = 0$ and 1 are only half of those of CH+D. Although its rotational distribution remains broader, the total ICS of CD+H becomes smaller than that of CH+D.

The branching-ratio inversion displayed in Fig. 3(b) is consistently reflected in the integral cross sections and product rotational distributions of the two product channels presented in Figs. 2 and 4. In Fig. 2 the CD+H dominance is seen to weaken progressively as J

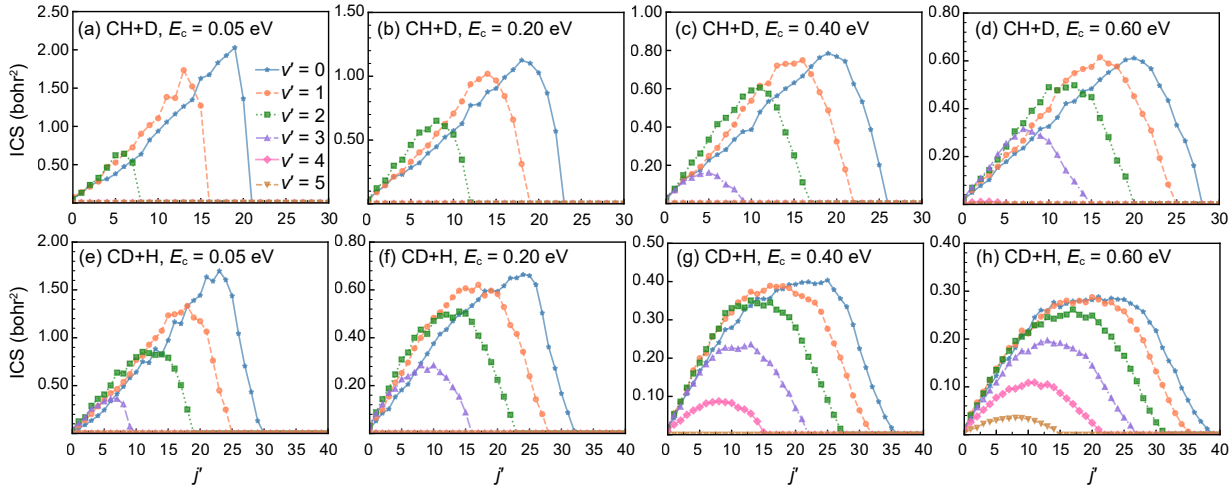

Fig. 4. Rovibrational state-resolved ICSs for the C(^{1}D)+HD → CH+D [(a)–(d)] and C(^{1}D)+HD → CD+H [(e)–(h)] reactions at collision energies of E_c = 0.05, 0.20, 0.40, and 0.60 eV.

increases from 10 to 50, and as Figs. 4(d) and 4(h) show, at the high collision energy E_c = 0.60 eV the CD+H channel retains a broader product rotational distribution yet yields a total ICS smaller than that of CH+D. Below we discuss the physical mechanism underlying this branching-ratio inversion. At low collision energies the reaction is dominated by low partial waves ($J \le 20$), and the CD+H channel is favored for three reasons. First, under these conditions the reaction is statistical in nature, and the CD+H channel is preferred because it possesses a larger number of open channels [12,40,44]. Second, the center of mass of HD lies asymmetrically, being closer to D than to H. As a result, the incoming C atom has a wider cone of acceptance for attacking the D side than for attacking the H side, which biases the insertion geometry toward CD-forming configurations [45]. In addition to these single-surface statistical mechanisms, recent theoretical work has identified a conical-intersection-regulated intermediate (CI-R) on the coupled $\tilde{a}^1A'/\tilde{b}^1A''$ potential-energy surfaces that selectively activates the C-H bond through a shallow pre-reactive well, providing a non-statistical pathway beyond the purely adiabatic statistical picture and further enhancing the CD+H branching ratio [8,17]. As the collision energy increases, higher partial waves ($J \ge 30$) contribute increasingly to the total cross section. The accompanying rise in the centrifugal barrier reduces the effective depth of the insertion well and shortens the lifetime of the intermediate complex [40,42]. Under these non-statistical conditions, channel competition is governed increasingly by dynamical constraints. Because the D atom is heavier than H and thus lies closer to the center of mass in the dissociating H-C-D framework, the CH+D product channel has the larger reduced mass. At large total angular momentum J, a larger reduced mass yields the lower centrifugal barrier. The release of the heavier D atom is thus dynamically favored, biasing the outcome toward the CH+D product channel.

Figures 5(a) and 5(b) present the vibrationally resolved ICSs for the CH+D and CD+H channels. With increasing collision energy, both channels populate progressively higher product vibrational states. At low collision energies ($E_c \le 0.10$ eV) the CD+H channel exhibits larger ICSs for $v' = 0$, 1, and 2 and additionally populates the $v' = 3$ product vibrational state, whereas the CH+D channel is confined mainly to $v' = 0$ and 1. As the collision energy increases, the two channels develop distinctly different vibrational distributions. For CH+D the $v' = 0$ state remains the dominant product throughout and the $v' = 1$ contribution is also substantial, together accounting for approximately two-thirds of the total ICS even at E_c = 0.60 eV, whereas higher vibrational states ($v' = 4$ and 5) are only weakly populated. For CD+H, by contrast, the vibrational distribution is much broader. Its $v' = 4$ state opens near 0.20 eV and $v' = 5$ near 0.44 eV, and these higher states are appreciably populated at elevated collision energies.

Figures 6(a) and 6(b) present the DCSs for the two product channels of the C+HD reaction at selected collision energies (0.05, 0.20, 0.40, and 0.60 eV). As shown in the figures, for both the CH+D and CD+H channels, the DCSs at the four collision energies are concentrated around the extreme scattering angles (0° and 180°) and are approximately forward-backward symmetric. This characteristic originates from the deep potential well along the reaction path, which supports long-lived intermediate complexes, indicating that the reaction proceeds predominantly via a complex-forming mechanism. Further analysis of the collision energy effect reveals the following. For the CH+D channel, at the low collision energy of 0.05 eV, the sideways scattering intensity is significantly higher than that at higher collision energies, while the forward and backward scattering intensities are considerably lower. In the higher collision energy range (0.20, 0.40, and 0.60 eV), the DCS increments for forward and backward scattering with increasing collision energy are substantially larger than those for sideways scattering. For the CD+H channel, as the collision energy

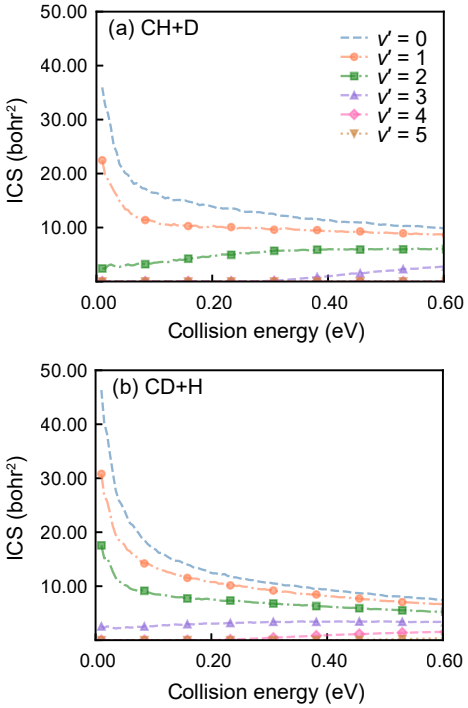

Fig. 5. The vibrational state-resolved integral cross sections of the two product channels. (a) denotes the CH+D product channel and (b) represents the CD+H product channel.

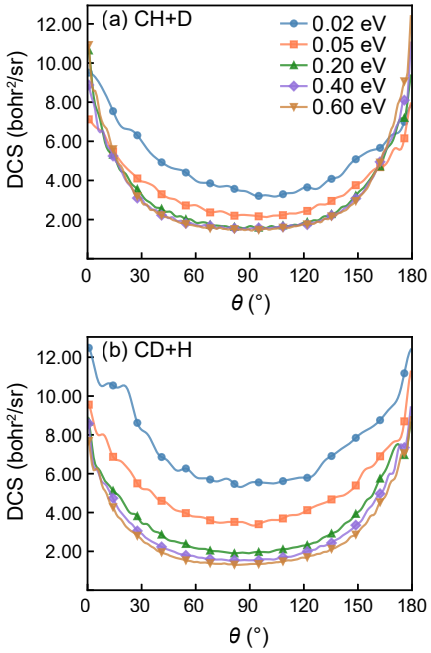

Fig. 6. The total DCSs for the two channels of the C(^{1}D)+HD ($v = 1, j = 2$) → CD/CH+D/H reaction at four selected collision energies. (a) denotes the CH+D product channel and (b) represents the CD+H product channel.

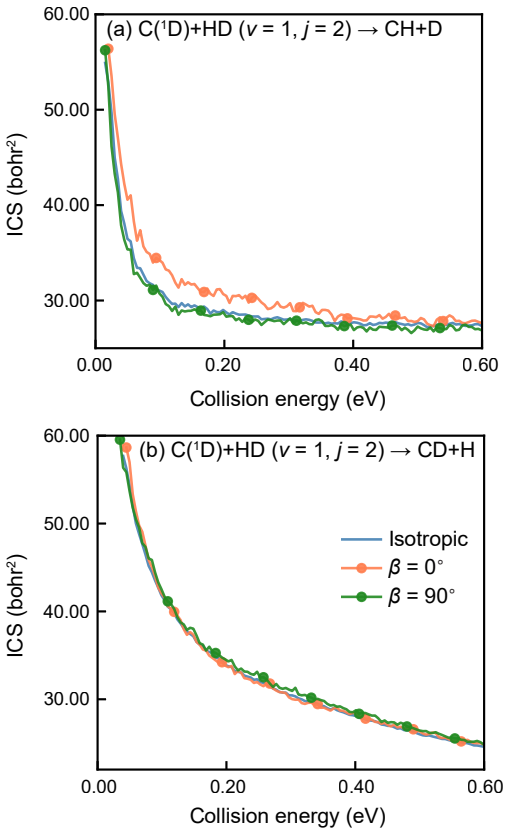

Fig. 7. Total ICSs as a function of collision energy for the C(^{1}D)+HD ($v = 1, j = 2$) reaction, corresponding to different initial alignments of the HD molecule ($\beta = 0°$, 90°) and the isotropic case. (a) denotes the CH+D product channel and (b) represents the CD+H product channel.

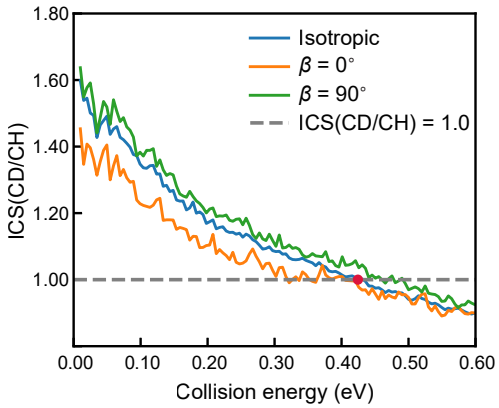

Fig. 8. Cross-section branching ratio (CD/CH) of the C(^{1}D)+HD ($v = 1, j = 2$) reaction as a function of collision energy for different stereodynamical configurations ($\beta = 0°$ and 90°) and isotropic case.

increases, the DCS at all scattering angles exhibits an overall decreasing trend. Notably, in contrast to the CH+D channel, the differences in sideways scattering intensity among different collision energies are more pronounced for the CD+H channel, whereas the differences in forward and backward scattering intensities are relatively small. These results indicate that, especially in the higher collision energy range, the forward and backward scattering of the CH+D channel are more strongly affected by the collision energy, while the sideways scattering intensity of the CD+H channel is more strongly affected.

Since the experimental techniques to produce HD ($v = 1, j = 2$) are relatively mature [23,26], we adopt an elevated initial vibrational state for HD molecules. Furthermore, the isotropic case serves as the unperturbed baseline, representing the collision process without any control imposed on the rotational state j. Its result corresponds to summing over all final m' values and averaging over all $2j+1$ initial m values [39]. This section focuses on the dynamical characteristics under stereodynamical control. We adopt the isotropic ICS as the benchmark: ICSs under different stereodynamical configurations exceeding this value indicate reaction promotion, while those lower than it indicate reaction suppression. Figure 7 presents the total ICS for the CH+D and CD+H channels of the C(^{1}D)+HD ($v = 1, j = 2$) reaction within the collision energy range of 0.01–0.60 eV, with curves for isotropic (blue), perpendicular (green) and parallel (orange) stereodynamical configurations. Different stereodynamical configurations clearly modulate the reactivity of the two channels differently. For CH+D, the parallel configuration consistently promotes the reaction (especially at low energies), while the perpendicular configuration slightly suppresses reactivity relative to the isotropic case. For CD+H, the parallel configuration weakly enhances reactivity only at low energies, and the perpendicular configuration provides mild enhancement at high energies. Stereodynamical control is substantially stronger for the CH+D channel than for the CD+H channel. The stereodynamical features displayed in the figure can be attributed to the nonpolar nature of the HD molecule. Because its steering interaction during the reaction is weak, the molecular orientation would otherwise be random in the absence of external alignment. Consequently, the artificially imposed alignment affects the reactivity [26].

To reveal how initial stereodynamical configurations modulate channel competition, the CD/CH branching ratio is examined as a function of collision energy and presented in Fig. 8. Under isotropic conditions, CD+H dominates at low collision energies, while CH+D becomes dominant above $E_c = 0.43$ eV. Stereodynamical control strongly modifies this competition: the parallel configuration ($\beta = 0°$) reduces the CD/CH branching ratio at a given collision energy, lowers the critical energy for CH channel dominance, and significantly enhances the competitive advantage of the CH product. In contrast, the perpendicular configuration ($\beta = 90°$) elevates the branching ratio, increases the critical energy for the CH channel to become dominant, and weakens the competitive advantage of the CH product.

Figure 9 shows the total DCS as a function of the scattering angle for the C+HD ($v = 1, j = 2$) reaction under different collision configurations at collision energies of 0.20 eV and 0.60 eV. For the CH+D channel [Panels (a) and (c)], the parallel configuration significantly

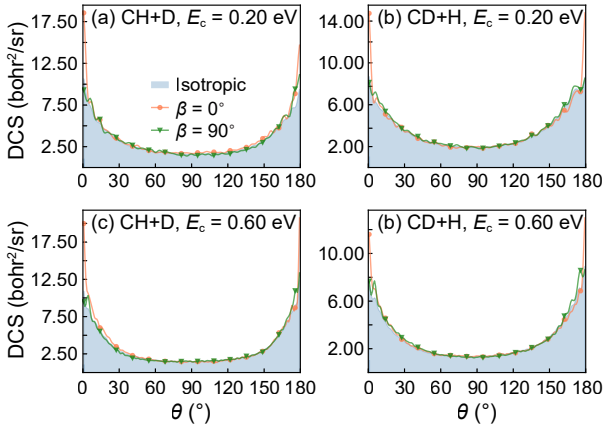

Fig. 9. Total DCSs for the perpendicular (green) and parallel (orange) stereodynamical configurations and isotropic case of the reaction C(^{1}D)+HD ($v = 1, j = 2$) as a function of scattering angle at $E_c = 0.20$ and 0.60 eV. (a) and (c) denotes the CH+D product channel and (b) and (d) represents the CD+H product channel.

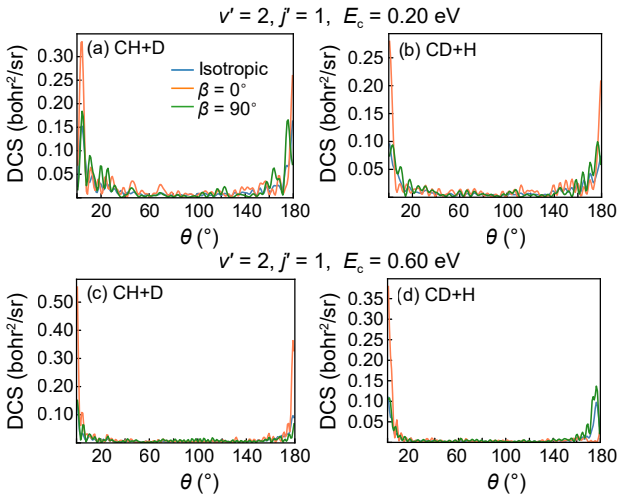

Fig. 10. The DCSs of the C(^{1}D)+HD ($v = 1, j = 2$) → CH ($v' = 2, j' = 1$) + D [(a), (c)] and C(^{1}D)+HD ($v = 1, j = 2$) → CD ($v' = 2, j' = 1$) + H [(b), (d)] reactions at $E_c = 0.20$ and 0.60 eV for different stereodynamical configurations ($\beta = 0°$ and 90°) and isotropic case.

enhances the extreme forward ($\theta = 0°$) and backward ($\theta = 180°$) scattering intensities. At 0.20 eV and 0.60 eV, the forward scattering intensities are enhanced by factors of 1.74 and 1.83, respectively, compared to the isotropic case, while the backward scattering intensities are enhanced by factors of 1.56 and 1.67, respectively. This promotional effect becomes stronger with increasing collision energy. The perpendicular configuration suppresses forward scattering and has only a weak promotional effect on backward scattering (factors of 1.19 and 1.08), which diminishes as the collision energy increases. In the forward ($\theta < 10°$) and backward ($\theta > 170°$) angular regions, the scattering peaks for both configurations shift toward the extreme scattering angles and become sharper with increasing collision energy. For the CD+H channel [Panels (b) and (d)], the parallel configuration also enhances the extreme forward and backward scattering, but the promotional effect weakens as the collision energy increases. At 0.20 eV and 0.60 eV, the forward scattering intensities are enhanced by factors of 1.69 and 1.51, respectively, and the backward scattering intensities by factors of 1.71 and 1.46, respectively. The perpendicular configuration exhibits suppression for both forward and backward scattering. In the forward region ($\theta < 10°$), a distinct DCS peak appears for the perpendicular configuration; this peak shifts toward the extreme scattering angle and becomes sharper with increasing collision energy. In contrast, the scattering peak for the parallel configuration shifts toward larger scattering angles and becomes broader. In contrast to direct reactions such as H+HD [26] and Br+H_2 [46], which typically exhibit a stereodynamical enhancement at sideways ($\theta \approx 90°$) scattering, the present deep-well insertion reaction yields products predominantly and symmetrically in the forward and backward scattering directions, thereby weakening the manifestation of the initial reactant alignment at sideways angles.

Figure 10 shows the DCS of the $v' = 2, j' = 1$ rovibrational product versus scattering angle (θ) at $E_c = 0.20$ and 0.60 eV. Panels (a) and (c) correspond to the CH+D channel at 0.20 and 0.60 eV, respectively; panels (b) and (d) correspond to the CD+H channel at the same energies. At $E_c = 0.20$ eV, CH+D scattering signals concentrate in forward ($\theta < 10°$) and backward ($\theta > 170°$) regions with sharp peaks, and the parallel configuration enhances forward intensity. At $E_c = 0.60$ eV, peaks of both configurations shift to extreme angles and sharpen, consistent with Fig.9. For CD+H at $E_c = 0.20$ eV, sharp forward and backward peaks appear with symmetry similar to CH+D but different configuration-dependent intensity modulation. At $E_c = 0.60$ eV, the perpendicular configuration forms stable sharp peaks shifting to extreme angles; the parallel configuration slightly enhances forward peaks but significantly reduces backward intensity. These rovibrationally resolved results demonstrate that stereodynamical configuration can control reaction outcomes at the state-to-state level.

Conclusion

In summary, this work performed TDWP dynamics calculations on the C(^{1}D)+HD ($v = 1, j = 2$) reaction using the newly developed global PES for $CH_2(\tilde{a}^1A')$. The reaction probabilities at $J = 0$ show no threshold and exhibit pronounced resonant oscillations for both product channels, confirming that the reaction proceeds via a long-lived complex-forming mechanism. With increasing partial wave quantum number J, centrifugal barriers gradually suppress the well confinement, smoothing out resonances and introducing a reaction threshold. The total ICS reveals a pronounced competition between the two channels, which is strongly dependent on the collision energy. At low energies, the CD+H channel dominates due to low partial wave contributions. Above 0.43 eV, high partial waves favor the CH+D channel, eventually reversing the product dominance. The CD/CH branching ratio displays oscillatory structure and decreases with collision energy, indicating a complex intramolecular isotope effect distinct from earlier reports. We speculate that this discrepancy arises from the modulation effect of reactant vibrational and rotational excitation.

Stereodynamical control selectively modulates the two product channels. The parallel alignment consistently promotes CH+D, especially at low energies, while the perpendicular alignment weakly suppresses this channel. DCS retain forward-backward symmetry under all alignments, confirming the complex-forming mechanism. The parallel configuration enhances extreme forward and backward scattering, whereas perpendicular alignment induces more intricate regulation. These results reveal the impact of stereodynamical control on insertion reactions and are expected to inspire further experimental and theoretical studies.

Acknowledgements

This work was supported by the National Natural Science Foundation of China (Grant No. 12374226).

References

[1] Gao S, Wei W, Zheng B, Song Y, and Meng Q 2014 *Int. J. Quantum Chem.* **114** 748
[2] Yuan J, Cheng D, and Chen M 2014 *RSC Adv.* **4** 36189
[3] Lu D and Guo H 2023 *J. Phys. Chem. A* **127** 3190
[4] De Fazio D, Aquilanti V, Cavalli S, Aguilar A, and Lucas J M 2006 *J.*

Chem. Phys. **125** 133109
[5] Guo H 2012 *Int. Rev. Phys. Chem.* **31** 1
[6] González-Lezana T 2007 *Int. Rev. Phys. Chem.* **26** 29
[7] Shen Z, Ma H, Zhang C, Fu M, Wu Y, Bian W, and Cao J 2017 *Nat. Commun.* **8** 14094
[8] Wu Y, Cao J, Ma H, Zhang C, Bian W, Nunez-Reyes D, and Hickson K M 2019 *Sci. Adv.* **5** eaaw0446
[9] Fisher W H, Carrington T, Sadowski C M, and Dugan C H 1985 *Chem. Phys.* **97** 433
[10] Sato K, Ishida N, Kurakata T, Iwasaki A, and Tsunashima S 1998 *Chem. Phys.* **237** 195
[11] Bussery-Honvault B, Honvault P, and Launay J M 2001 *J. Chem. Phys.* **115** 10701
[12] Lin S Y and Guo H 2004 *J. Chem. Phys.* **120** 9907
[13] Defazio P, Gamallo P, González M, Akpinar S, Bussery-Honvault B, Honvault P, and Petrongolo C 2010 *J. Chem. Phys.* **132** 104306
[14] Joseph S, Caridade P J S B, and Varandas A J C 2011 *J. Phys. Chem. A* **115** 7882
[15] Zhang C, Fu M, Shen Z, Ma H, and Bian W 2014 *J. Chem. Phys.* **140** 234301
[16] Sun Z, Zhang C, Lin S, Zheng Y, Meng Q, and Bian W 2013 *J. Chem. Phys.* **139** 014306
[17] Wu Y, Cao J, and Bian W 2020 *J. Phys. Chem. A* **124** 801
[18] Liu R, Yuan Y, Xing W, and Li W 2026 *Int. J. Quantum Chem.* **126** e70138
[19] Zare R N 1988 *Angular Momentum: Understanding Spatial Aspects in Chemistry and Physics* (New York: Wiley)
[20] Liu K 2015 *J. Chem. Phys.* **142** 080901
[21] Loesch H J 1995 *Annu. Rev. Phys. Chem.* **46** 555
[22] Zare R N 1982 *Ber. Bunsenges. Phys. Chem.* **86** 422
[23] Mukherjee N and Zare R N 2011 *J. Chem. Phys.* **135** 024201
[24] Perreault W E, Mukherjee N, and Zare R N 2019 *J. Chem. Phys.* **150** 174301
[25] Mukherjee N 2023 *J. Phys. Chem. A* **127** 418
[26] Wang Y, Huang J, Wang W, Du T, Xie Y, Ma Y, Xiao C, Zhang Z, Zhang D H, and Yang X 2023 *Science* **379** 191
[27] Kang L 2011 *Int. J. Quantum Chem.* **111** 117
[28] Perreault W E, Mukherjee N, and Zare R N 2017 *Science* **358** 356
[29] Li W, Zhang D H, and Sun Z 2014 *J. Phys. Chem. A* **118** 9801
[30] Light J C, Hamilton I P, and Lill J V 1985 *J. Chem. Phys.* **82** 1400
[31] Feit M D, Fleck J A, and Steiger A 1982 *J. Comput. Phys.* **47** 412
[32] Colbert D T and Miller W H 1992 *J. Chem. Phys.* **96** 1982
[33] Zhao H, Hu X, Xie D, and Sun Z 2018 *J. Chem. Phys.* **149** 174103
[34] Manolopoulos D E 1986 *J. Chem. Phys.* **85** 6425
[35] Brouard S, Macias D, and Muga J G 1994 *J. Phys. A: Math. Gen.* **27** L439
[36] Sun Z, Guo H, and Zhang D H 2010 *J. Chem. Phys.* **132** 084112
[37] Li X and Sun Z 2018 *Theor. Chem. Acc.* **137** 19
[38] Sun Z, Zhang D H, and Lee S Y 2009 *J. Phys. Chem. A* **113** 4145
[39] Da Silva H, Kendrick B K, and Balakrishnan N 2022 *J. Chem. Phys.* **156** 044305
[40] Lin S Y and Guo H 2004 *J. Chem. Phys.* **121** 1285
[41] Gogtas F, Bulut N, and Akpinar S 2005 *Int. J. Quantum Chem.* **105** 478
[42] Sun Z P, Zhao W K, and Yang C L 2017 *Int. J. Quantum Chem.* **117** e25431
[43] Kang L, Zhang S, Zhu M, and Dai B 2011 *Can. J. Chem.* **89** 1283
[44] Zhang C, Zheng Y, Cao J, and Bian W 2017 *RSC Adv.* **7** 34348
[45] Zhang J, Gao S B, Wu H, and Meng Q T 2015 *J. Phys. Chem. A* **119** 8959
[46] Xu X, Buren B, and Chen M 2025 *J. Phys. Chem. A* **129** 6572